JOURNAL OF GUIDANCE, CONTROL, AND DYNAMICS
Vol. 32, No. 4, July–August 2009

Extracting Energy from Downdraft to Enhance Endurance of Uninhabited Aerial Vehicles

Yiyuan J. Zhao*
University of Minnesota, Minneapolis, Minnesota 55455

DOI: 10.2514/1.42133

The ability of uninhabited aerial vehicles to perform drastic maneuvers enables them to benefit from wind profiles that may be unfavorable to inhabited aircraft. This paper examines optimal uninhabited aerial vehicle flights that can extract energy from downdrafts for enhancing endurance. Uninhabited aerial vehicle motions are described by a point-mass dynamic model. A downdraft wind field is modeled by a pair of three-dimensional vortex rings placed symmetrically with respect to the ground. Fundamental dimensionless parameters that affect uninhabited aerial vehicle behaviors in a downdraft are identified through the normalization of the equations and wind expressions. Uninhabited aerial vehicle flight through a downdraft is formulated as a nonlinear optimal control problem that minimizes the average thrust or power per unit time. Vehicle performance and operational limits are enforced through boundary conditions and path constraints. These optimal control problems are converted into parameter optimization problems with a collocation method and solved numerically using the sparse parameter optimization software SNOPT. Numerical solutions systematically obtained for a range of dimensionless parameters reveal four basic patterns of optimal uninhabited aerial vehicle flights through a downdraft in the vertical plane. Results demonstrate that traditional definitions of favorable winds may need to be revised for uninhabited aerial vehicles.

Nomenclature

C_{D_0}	=	zero-lift drag coefficient
(C_L, C_D)	=	(lift, drag) coefficients
D	=	aerodynamic drag
$E_{\max}$	=	maximum lift-to-drag ratio or aerodynamic efficiency
g	=	gravitational acceleration
H	=	height of the vortex ring
h	=	inertial altitude
I	=	performance index
K	=	induced drag factor
L	=	aerodynamic lift
m	=	aircraft mass
N	=	number of nodes in the discretization of time interval
n	=	load factor
P	=	power
R	=	vortex ring radius
S	=	vehicle reference area
T	=	engine thrust
t	=	time
V	=	airspeed
(W_x, W_y, W_h)	=	(east, north, up) wind component
(x, y)	=	(east, north) position
Γ	=	ring-vortex intensity
γ	=	air-relative flight path angle
μ	=	bank angle
ρ	=	air density
τ	=	normalized time
Ψ	=	heading angle measured clockwise from the north

Subscripts

f	=	final value
0	=	initial value

Superscripts

r	=	reference value
$\bar{}$	=	normalized variable
$\dot{}$	=	time derivative
$'$	=	derivative with respect to normalized time

I. Introduction

UNINHABITED aerial vehicles (UAVs) are finding increasingly more applications in a wide range of areas where human presence is inconvenient, expensive, or dangerous. In many UAV applications such as surveillance, long flight endurances are highly desirable. Therefore, it is important to consider all possible means for their enhancements. This paper studies energy extraction from a seemingly unfavorable wind pattern for improving UAV flight endurances.

Wind energy has been used to improve flight performances for all types of aircraft. In particular, a sailplane uses vertically rising thermals to achieve long flight distances [1–6], which can also be used by UAVs [7]. Low-altitude wind gradients can be exploited to facilitate a self-perpetuating flight pattern known as dynamic soaring [8–11]. These studies establish both characteristics and potential benefits of optimal energy extraction from wind patterns that are commonly defined to be favorable.

However, downdraft has traditionally been considered unfavorable, even dangerous, for inhabited flights. Indeed, the downward flow can cause an aircraft to lose altitude, and the accompanying wind shear can cause an aircraft to lose airspeed. Past studies of commercial aircraft flights through downdrafts focus on avoidance or safe penetration if avoidance cannot be achieved [12–17]. On the other hand, UAVs can fly much more drastic maneuvers because they do not have humans on board. In addition, their typically smaller sizes and lighter weights make them more susceptible to winds and more able to benefit from wind energy. It is plausible that they may be able to take advantage of traditionally unfavorable wind patterns. The idea of extracting energy from downdrafts is postulated by Kiceniuk [18].

Received 11 November 2008; revision received 6 January 2009; accepted for publication 10 January 2009.

*Professor, Aerospace Engineering and Mechanics; gyyz@aem.umn.edu. Associate Fellow AIAA.

This paper studies fundamental patterns of optimal UAV flights through downdrafts and their potential fuel-saving benefits. It shows that under appropriate conditions, UAVs are indeed capable of exploiting wind energies in a downdraft to enhance endurance. By demonstrating the potential to enhance endurance through downdrafts, this paper suggests that the concept of "favorable winds" needs to be refined for UAV flights.

Technological advances over the last several decades have made it feasible to use wind energy in practical UAV flights. Joe Wurts† [19] demonstrated dynamic soaring of a radio-controlled aircraft toward the end of the 1990s. Boslough presented instrumented flight tests of UAV dynamic soaring that unambiguously shows the feasibility of dynamic soaring in sustaining UAV flight [19]. Michael Allen† used a hand-launched UAV to validate the benefit of heat thermals to extend flight time [20]. On 18 April 2008, Dan Edwards† set a new world's record for an autonomous glider flying using thermals.

In the remainder of this paper, a downdraft flow is modeled by a pair of three-dimensional vortex rings that are placed symmetrically with respect to the ground. A set of three-dimensional point-mass equations is used to describe UAV dynamic motions. For good numerical efficiency as well as for gaining physical insights, these equations and wind expressions are normalized. A set of fundamental dimensionless parameters are identified that inherently govern the behaviors of a UAV flight through a downdraft. UAV flights for maximizing endurance are formulated as nonlinear optimal control problems that minimize the average thrust or power per unit time, depending on the nature of the power plant in the UAV. Appropriate boundary conditions as well as path constraints arising from UAV performance and operational limitations are imposed. These optimal control problems are approximated by parameter optimization via a collocation approach. The sparse optimization software package SNOPT is used to obtain extensive numerical solutions.

II. Downdraft Modeling

A representative occurrence of downdrafts is found in a weather phenomenon known as downburst [21]. A downburst is a mass of cold air that descends to the ground in a column. As the wind approaches the ground, the wind changes its direction and radiates outward. A downburst usually picks up dust and dirt and may be visually detected. Doppler radar is able to look through a downburst and measure its air movement [22].

A mathematical model of the downburst flow velocity is needed for studying energy-efficient UAV flights through it. The classical literature presents a ring-vortex model [23]. In this model, the stream function of a three-dimensional, irrotational, and incompressible ring-vortex flowfield is expressed through complete elliptic integrals of the first and second kinds, as functions of the least and the greatest distance from a point of interest to the ring filament. To achieve zero vertical velocity at the ground, a secondary, imaginary ring of equal intensity has to be placed symmetrically below the ground to make the Earth's surface a stream surface (Fig. 1). The flow velocity is then obtained by differentiating the sum of the two stream functions.

However, these elegant expressions suffer from two drawbacks. Computations of flow velocities require differentiations of the complete elliptic integrals and can be slow for an iterative optimization process. In addition, as the point of interest approaches the central filament of the primary vortex ring, these expressions predict infinitely large speeds. In reality, viscous stresses dominate the region close to the central filament, and the velocities are finite.

Zhao in [24] presents approximate analytical expressions directly for wind velocities induced by a pair of ring vortices. In addition, these expressions predict finite velocities as the point of interest approaches the central filament of the primary ring. Specifically, the wind velocity components for a primary vortex ring located at (0, 0, H) are given by

$$W_x = \frac{x}{r} W_m \left[\frac{h_p/r_{2p} - h_p/r_{1p}}{\sqrt{r^2 + h_p^2 + R^2}} - \frac{h_m/r_{2m} - h_m/r_{1m}}{\sqrt{r^2 + h_m^2 + R^2}} \right] \tag{1}$$

†Lu, P., private communication, Dec. 2008.

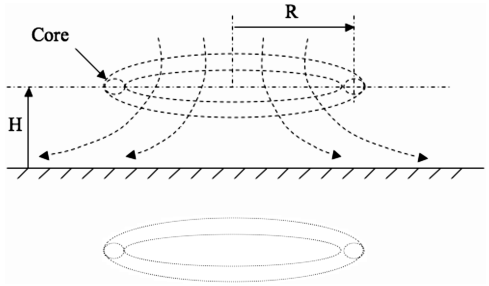

Fig. 1 A three-dimensional ring-vortex downburst model.

$$W_y = \frac{y}{r} W_m \left[\frac{h_p/r_{2p} - h_p/r_{1p}}{\sqrt{r^2 + h_p^2 + R^2}} - \frac{h_m/r_{2m} - h_m/r_{1m}}{\sqrt{r^2 + h_m^2 + R^2}} \right] \tag{2}$$

$$W_h = \frac{4}{3} W_m \left[\frac{r_1/r_{1p}^{3/4} - r_2/r_{2p}^{3/4}}{(0.25r^2 + h_p^2 + R^2)^{3/4}} - \frac{r_1/r_{1m}^{3/4} - r_2/r_{2m}^{3/4}}{(0.25r^2 + h_m^2 + R^2)^{3/4}} \right] \tag{3}$$

$$W_m = \frac{1.182\Gamma R}{2\pi} \left(1 - e^{-\frac{r_{1p}}{R_c^2}} \right) \tag{4}$$

where

$$r = \sqrt{x^2 + y^2}, \qquad r_1 = r - R, \qquad r_2 = r + R \tag{5}$$

$$h_p = h - H, \qquad h_m = h + H \tag{6}$$

$$r_{1p} = r_1^2 + h_p^2, \qquad r_{2p} = r_2^2 + h_p^2 \tag{7}$$

$$r_{1m} = r_1^2 + h_m^2, \qquad r_{2m} = r_2^2 + h_m^2 \tag{8}$$

Figure 2 shows representative wind profiles across a downburst at four selected altitudes, two below the primary vortex ring and two above the ring. In all cases, the vertical wind exhibits a small updraft at the outer side of the vortex ring and becomes a strong downdraft over the central part of the ring. Below the ring, the horizontal wind changes from a headwind to a tailwind, whereas above the ring, it changes from a tailwind to a headwind. Magnitudes of both the horizontal and vertical wind profiles vary with altitudes.

In this paper, the downburst wind field is assumed stationary. As a result, for $z = x$, y, or h, the wind rate of change is caused by aircraft motion and is given by

$$\dot{W}_z = \frac{\partial W_z}{\partial x} \dot{x} + \frac{\partial W_z}{\partial y} \dot{y} + \frac{\partial W_z}{\partial h} \dot{h} \tag{9}$$

III. Equations of Motion and Fundamental Performance Parameters

For trajectory optimization across a downburst, UAV motions can be adequately represented by a three-dimensional point-mass model assuming a flat Earth. The corresponding equations of motion are summarized for convenience [25–28]:

$$\dot{V} = (T - D)/m - g \sin\gamma - \dot{W}_x \cos\gamma \sin\Psi - \dot{W}_y \cos\gamma \cos\Psi - \dot{W}_h \sin\gamma \tag{10}$$

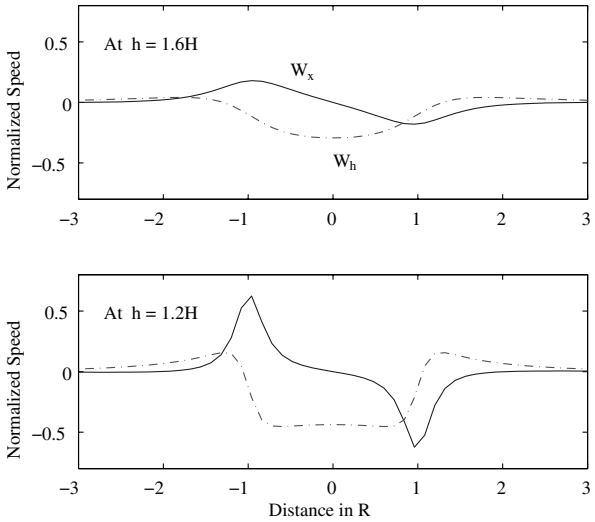

a)

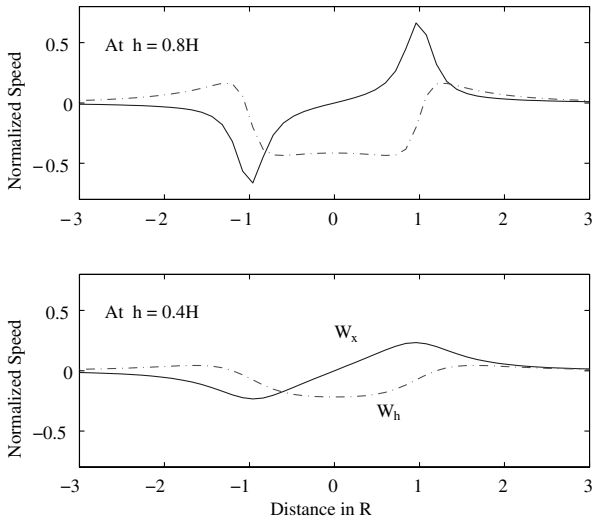

b)

Fig. 2 Wind profiles across a downburst a) above the ring and b) below the ring.

$$V\cos\gamma\dot{\Psi} = L\sin\mu/m + \dot{W}_x\cos\Psi - \dot{W}_y\sin\Psi \tag{11}$$

$$V\dot{\gamma} = L\cos\mu/m - g\cos\gamma + \dot{W}_x\sin\gamma\sin\Psi + \dot{W}_y\sin\gamma\cos\Psi - \dot{W}_h\cos\gamma \tag{12}$$

$$\dot{h} = V\sin\gamma + W_h \tag{13}$$

$$\dot{x} = V\cos\gamma\cos\Psi + W_x \tag{14}$$

$$\dot{y} = V\cos\gamma\sin\Psi + W_y \tag{15}$$

In these equations, the UAV mass m is assumed constant. The lift and drag forces can be expressed as

$$L = \tfrac{1}{2}\rho V^2 S C_L, \qquad D = \tfrac{1}{2}\rho V^2 S C_D \tag{16}$$

and the drag coefficient is modeled by the drag polar [28]

$$C_D = C_{D_0} + KC_L^2 \tag{17}$$

where the induced drag factor K can be determined from the aerodynamic efficiency $E_{\max}$ and the zero-lift drag coefficient C_{D_0} as

$$K = \frac{1}{4E_{\max}^2 C_{D_0}} \tag{18}$$

To obtain good numerical efficiency in the optimization process, the above equations are normalized as follows. Define

$$\bar{V} = \frac{V}{\sqrt{gR}}, \qquad (\bar{x},\bar{y},\bar{h}) = \frac{(x,y,h)}{R}, \qquad \bar{T} = \frac{T}{mg} \tag{19}$$

$$\tau = \sqrt{\frac{g}{R}}t, \qquad ()' \triangleq \frac{d()}{d\tau} \tag{20}$$

$$\bar{W}_{x,y,h} = \frac{W_{x,y,h}}{\sqrt{gR}}, \qquad \bar{W}'_{x,y,h} = \frac{\dot{W}_{x,y,h}}{g} \tag{21}$$

The set of normalized equations can be expressed as

$$\bar{V}' = \bar{T} - \bar{\rho}\bar{V}^2(C_{D_0} + KC_L^2) - \sin\gamma - \bar{W}'_x\cos\gamma\sin\Psi - \bar{W}'_y\cos\gamma\cos\Psi - \bar{W}'_h\sin\gamma \tag{10a}$$

$$\Psi' = \bar{\rho}\,\bar{V}\frac{C_L\sin\mu}{\cos\gamma} + \frac{1}{\bar{V}\cos\gamma}(\bar{W}'_y\sin\Psi - \bar{W}'_x\cos\Psi) \tag{11a}$$

$$\gamma' = \bar{\rho}\,\bar{V}\,C_L\cos\mu - \frac{\cos\gamma}{\bar{V}} + \frac{1}{\bar{V}}(\bar{W}'_x\sin\gamma\sin\Psi + \bar{W}'_y\sin\gamma\cos\Psi - \bar{W}'_h\cos\gamma) \tag{12a}$$

$$\bar{h}' = \bar{V}\sin\gamma + \bar{W}_h \tag{13a}$$

$$\bar{x}' = \bar{V}\cos\gamma\sin\Psi + \bar{W}_x \tag{14a}$$

$$\bar{y}' = \bar{V}\cos\gamma\cos\Psi + \bar{W}_y \tag{15a}$$

The above normalization process exposes a few dimensionless parameters that represent the fundamental performance capabilities of an aerial vehicle flying through a downburst. A normalized air density is given by

$$\bar{\rho} = \frac{\rho g R}{2(mg/S)} \tag{22}$$

Normalized intensity and scale of the downburst are given by

$$\bar{\Gamma} = \frac{\Gamma}{R\sqrt{gR}}, \qquad \bar{H} = \frac{H}{R} \tag{23}$$

There are five fundamental dimensionless parameters that govern UAV flights through a downdraft: $\bar{\rho}$, $\bar{\Gamma}$, $\bar{H}$, C_{D_0}, and $E_{\max}$. $\bar{\rho}$ combines effects of the atmospheric density ρ, wing loading mg/S, and the radius of the downburst ring R. A smaller $\bar{\rho}$ corresponds to a larger wing loading, thus a heavier UAV, a smaller vortex ring, and/or thinner air, and vice versa. In comparison, $\bar{\Gamma}$ represents a normalized downburst intensity, and $\bar{H}$ represents the closeness of

the downburst to the ground. Finally, C_{D_0} and $E_{\max}$ depend on UAV aerodynamic design and manufacturing.

IV. Problem Formulations

It is conceivable that the downdraft may potentially be used to accelerate a UAV downward to increase its kinetic energy. This increase in kinetic energy may then be translated in a UAV flight to maximize endurance, to maximize range capability, and/or to minimize flight time across the region. In this paper, the enhancement of endurance through downdraft energy is studied.

For a jet-engined UAV, the minimum fuel consumption corresponds to the minimum thrust required [29]. Flight endurance can be enhanced by minimizing the average thrust required per unit time. Mathematically, an optimal control problem can be stated as

$$\min_{C_L,\mu,\bar{T},\bar{V}_0,\tau_f} I = \frac{1}{\tau_f}\int_0^{\tau_f} \bar{T}\,\mathrm{d}\tau \tag{24}$$

subject to Eqs. (10a), (11a), (12a), (13a), (14a), and (15a), appropriate initial conditions Ψ_0, γ_0, $\bar{h}_0$, $\bar{x}_0$, $\bar{y}_0$, and the following terminal conditions:

$$\bar{V}_f = \bar{V}_0, \qquad \Psi_f = \Psi_0, \qquad \gamma_f = \gamma_0 \tag{25}$$

$$\bar{h}_f = \bar{h}_0, \qquad \bar{x}_f = -\bar{x}_0, \qquad \bar{y}_f = \bar{y}_0 \tag{26}$$

These boundary conditions require that the UAV start and end at the same specified conditions before and after passing through the downburst. In this problem, $\bar{V}_0$ and τ_f are open parameters that are determined in the optimization process.

In comparison, fuel consumption for a propeller-driven UAV is directly related to its power required [29]. To maximize endurance, the optimal control problem is formulated to minimize the average power per unit flight time. Mathematically

$$\min_{C_L,\mu,\bar{T},\bar{V}_0,\tau_f} I = \frac{1}{\tau_f}\int_0^{\tau_f} \bar{T}\,\bar{V}\,\mathrm{d}\tau \tag{27}$$

subject to the same equations of motion in Eqs. (10a), (11a), (12a), (13a), (14a), and (15a), appropriate initial conditions, and the terminal constraints in Eqs. (25) and (26).

For both optimal control problems, the following path constraints on UAV states and controls are imposed to obtain physically meaningful trajectories

$$\bar{V}_{\min} \le \bar{V} \le \bar{V}_{\max}, \qquad |\gamma| \le \gamma_{\max} \tag{28}$$

$$0 \le \bar{h} \le \bar{h}_{\max} \tag{29}$$

$$|\mu| \le \mu_{\max}, \qquad C_{L_{\min}} \le C_L \le C_{L_{\max}} \tag{30}$$

In addition, a limitation on loading is specified as

$$n = \frac{L}{mg} = \bar{\rho}\bar{V}^2 C_L \le n_{\max} \tag{31}$$

Furthermore, for a jet-engined UAV, a maximum thrust bound is imposed as

$$0 \le \bar{T} \le \bar{T}_{\max} \tag{32}$$

whereas for a propeller-driven UAV, a constraint on the maximum power is imposed

$$0 \le \bar{P} = \bar{T}\,\bar{V} \le \bar{P}_{\max} \tag{33}$$

Finally, bounds on the time rates of control variables are imposed

$$|\bar{T}'| \le (\bar{T}')_{\max}, \qquad |C_L'| \le (C_L')_{\max}, \qquad |\mu'| \le (\mu')_{\max} \tag{34}$$

The benefit of extracting energy from a downburst may be compared with reference trajectories that do not actively take advantage of the wind energy. In this paper, two reference trajectories are introduced. The first represents a straight-line steady-state level flight at the constant speed that minimizes fuel consumption under zero wind, and at the altitude that is the same as the initial altitude in a dynamically optimized flight. For jet-engined UAVs, this reference trajectory is defined by

$$\bar{V}^{r1} = \frac{1}{\sqrt{2\bar{\rho}C_{D_0}E_{\max}}} \tag{35}$$

$$C_L^{r1} = 2C_{D_0}E_{\max} \tag{36}$$

$$I^{r1} = \bar{T}^{r1} = \frac{1}{E_{\max}} \tag{37}$$

and for propellor-driven vehicles,

$$\bar{V}^{r1} = \frac{1}{\sqrt{2\bar{\rho}\sqrt{3}\,C_{D_0}E_{\max}}} \tag{38}$$

$$C_{L_0}^{r1} = 2\sqrt{3}C_{D_0}E_{\max} \tag{39}$$

$$\bar{T}^{r1} = \frac{2}{\sqrt{3}E_{\max}} \tag{40}$$

$$I^{r1} = (\bar{T}\,\bar{V})^{r1} = \frac{1}{3}\sqrt{\frac{2\sqrt{3}}{\bar{\rho}C_{D_0}}}\frac{1}{\sqrt{E_{\max}^3}} \tag{41}$$

If the downdraft wind is severe, a judicious option would be to avoid it. The second reference trajectory represents a level turning avoidance trajectory in zero wind, in which the vehicle would first turn right at a specified bank angle, then turn left at an opposite bank angle of the same magnitude, and finally turn right again to align up to the original heading. The vehicle is assumed to be in a steady-state constant speed level flight throughout the turning process, and the constant speed is the optimal value for maximum endurance in the constant bank turn. For a jet-engined UAV,

$$\bar{V}^{r2} = \frac{1}{\sqrt{2\bar{\rho}C_{D_0}E_{\max}\cos\mu_t}} \tag{42}$$

$$C_L^{r2} = 2C_{D_0}E_{\max} \tag{43}$$

$$I^{r2} = \bar{T}^{r2} = \frac{1}{E_{\max}\cos\mu_t} \tag{44}$$

where μ_t is the reference bank angle. For a propeller-driven UAV,

$$\bar{V}^{r2} = \frac{1}{\sqrt{2\sqrt{3}\bar{\rho}C_{D_0}E_{\max}\cos\mu_t}} \tag{45}$$

$$C_L^{r2} = 2\sqrt{3}C_{D_0}E_{\max} \tag{46}$$

$$\bar{T}^{r2} = \frac{2}{\sqrt{3}E_{\max}\cos\mu_t} \tag{47}$$

$$I^{r2} = (\bar{T}\,\bar{V})^{r2} = \frac{1}{3}\sqrt{\frac{2\sqrt{3}}{\bar{\rho}C_{D_0}}}\frac{1}{\sqrt{E_{\max}^3\cos^3\mu_t}} \tag{48}$$

Note that the vehicle would use the same lift coefficient in this turn reference trajectory as in the first reference trajectory of a straight-line level flight. The extra lift needed during a turn is provided by a higher airspeed.

If $I^* < I^{r1}$, the downdraft represents an opportunity for energy extraction in enhancing endurance. If $I^* \geq I^{r1}$ but $I^* < I^{r2}$, the downdraft creates an unfavorable wind but it is still better to fly through it in an optimal manner than to avoid it. Finally if $I^* > I^{r2}$, it is better for the UAV to avoid the downdraft. In a surveillance flight, a UAV would circle around a given area. Once a downdraft is discovered, a UAV may repeatedly fly through it during its limited lifespan. A favorable downdraft field may provide significant enhancement to the UAV flight endurance over the duration of its existence.

V. Numerical Solution Methods

The above optimal control problems are solved numerically. Over the last several decades, numerous numerical schemes have been developed to solve nonlinear optimal control problems [30]. Particularly, the conversion of optimal control problems into parameter optimization through a collocation approach [31–36] offers flexibility, simplicity, and computational speed, and is used here. In this approach, both state and control variables are approximately represented by their values at a series of discrete time nodes.

There are different ways of approximating the differential equations and path constraints in the conversion process. In this paper, differential equations are enforced as a system of nonlinear constraints through a forward difference scheme at the discrete time nodes [33]. Boundary conditions in Eqs. (25) and (26) are enforced as linear constraints, direct constraints on solution variables are enforced as variable bounds, and the upper limit on the load factor in Eq. (31) is treated as a nonlinear constraint. An example conversion process can be found in [10].

Converted parameter optimization problems are solved with the software program SNOPT [37]. Analytical gradient expressions are provided for the cost functions, whereas gradients of the nonlinear constraints are determined numerically. Equally spaced nodes are used and different numbers of nodes N are experimented. Results presented below are obtained with $N = 51$ for a balance among solution accuracy, convergence, and computational speed. The feasibility and optimality tolerance levels are selected as $\epsilon_f = 10^{-8}$ and $\epsilon_o = 10^{-6}$. A solution in most cases takes about 50 to 100 iterations.

VI. Numerical Optimization Process

A downburst may last about 5–10 min and remain at its full intensity for about 5 min. It can create vertical winds up to 50 ft/s and, as it spreads out near the ground, horizontal winds up to 100 ft/s. In this paper, ranges of downburst parameters are assumed to be $\Gamma = 5000$–$250,000$ ft^2/s, $H = 0$–5000 ft, and $R =$ 500–5000 ft. Considering typical UAV wing loadings of $mg/S =$ 5–60 lb/ft^2, the following values of the fundamental dimensionless parameters are examined in the current study:

$$\bar{\rho} = 0.5\text{–}2 \tag{49}$$

$$\bar{\Gamma} = 0.01\text{–}4.0, \qquad \bar{H} = 0.5\text{–}2 \tag{50}$$

$$C_{D_0} = 0.015\text{–}0.035, \qquad E_{\max} = 10\text{–}35 \tag{51}$$

In addition, thrust and power bounds are assumed to be $\bar{T}_{\max} = 0.25$ and $\bar{P}_{\max} = 0.1 \times 550/\sqrt{gR}$, respectively, based on [38]. Other variable bounds are $C_{L_{\max}} = 1.2$, $C_{L_{\min}} = 0$, $n_{\max} = 3$, $\gamma_{\max} =$ 50 deg, $(\dot{C}_L)_{\max} = C_{L_{\max}}/4$, $(\dot{\bar{T}})_{\max} = \bar{T}_{\max}/4$ for a jet-engined UAV, and $(\dot{\bar{T}})_{\max} = \bar{T}_{\max}$ for a propeller-driven UAV.

The minimum airspeed limit is usually specified in reference to the stall speed. At steady-state flights,

$$\frac{1}{2}\rho V^2 S C_L = W \Rightarrow \bar{V}_{\rm ss} = \frac{1}{\sqrt{\bar{\rho}C_L}}$$

Allowing for the dynamic nature of flights through a downdraft, we select

$$\bar{V}_{\min} = \frac{0.8}{\sqrt{\bar{\rho}C_{L_{\max}}}} \tag{52}$$

In comparison, the maximum flight speed for a given aircraft can be affected by aerodynamic drag, thrust capability, and/or structural integrity, and a simple choice of its value is not obvious. In this paper, we assume that the maximum UAV airspeed is somewhat higher than a typical steady-state cruise speed

$$\bar{V}_{\max} = \frac{1.5}{\sqrt{\bar{\rho}C_{L_{\rm cr}}}} \tag{53}$$

where $C_{L_{\rm cr}}$ is a typical cruise lift coefficient, such as corresponding to an angle of attack of 3–5 deg, or $C_{L_{\rm cr}} = 2\pi(3\text{–}5 \text{ deg})$.

In the numerical optimization studies, it is found that the choice of the minimum airspeed limit does not affect the optimal trajectory significantly, whereas the choice of the maximum airspeed affects the smoothness of a trajectory and may even influence the optimal trajectories to take one pattern or another. For different choices of airspeed limits studied, the basic patterns of optimal flights discussed below remain the same.

In establishing initial trajectory conditions, it is assumed that the UAV is in a steady-state level flight when it encounters a downdraft and would pass through the horizontal center of the primary ring on its nominal path if there were no wind. Without loss of generality, it is further assumed that the UAV is initially flying due east

$$\Psi_0 = 90 \text{ deg}, \qquad \gamma_0 = 0, \qquad \bar{x}_0 = -3, \qquad \bar{y}_0 = 0 \tag{54}$$

Different values of $\bar{x}_0$ are studied and are found to not affect fundamental patterns of optimal flights. In contrast, different initial altitudes can result in different patterns of optimal flights. In the results presented next, the following range of $\bar{h}_0$ is considered:

$$\bar{h}_0 = (0.5\text{–}2)\bar{H} \tag{55}$$

In the systematic numerical solution process, it is more convenient to vary values of the dimensionless parameters such as $\bar{\rho}$ and $\bar{\Gamma}$ than to vary the radius of the ring R, which is used to normalize other variables in Eqs. (19–21). Actually, R is essentially a scaling factor in the normalized formulation. Its choice may affect the efficiency of the numerical solution process, but does not seem to fundamentally alter the patterns of optimal flights through a downburst. In the following, $R = 1000$ is used.

When interpreting the optimal trajectory results, on the other hand, the R values should be physically meaningful. Computed optimal trajectories exhibit peak airspeeds around $1.5V_c$ and occasionally $2V_c$, where $V_c = \sqrt{gR}$ is the normalizing speed in Eq. (19). As shown in Table 1, these represent maximum airspeeds of about 466.00–621.32 ft/s and Mach numbers of 0.417–0.556 for $R =$ 3000 and smaller values for smaller Rs. Therefore, the drag polar in Eq. (17) with constant coefficients is valid. For $R = 5000$ ft, the peak airspeed could reach 601.59–802.12 or Mach numbers of 0.5389–0.7186. These start to approach the drag divergence Mach number, but Eq. (17) with constant coefficients is still expected to be reasonable. For $R > 5000$, dependences of C_{D_0} and K on Mach number should be modeled. If the potential peak airspeed exceeds the performance capability of a UAV, it should try to avoid the downdraft.

Table 1 Normalizing time and speed at different *Rs*

R, ft	$t_c = \sqrt{R/g}$, s	$V_c = \sqrt{Rg}$, ft/s	$M_c = V_c/a$[a]
500	3.942	126.83	0.1136
1000	5.575	179.36	0.1606
3000	9.657	310.66	0.2781
5000	12.467	401.06	0.3591

[a]Based on sea level speed of sound of $a = 1116.94$ ft/s.

The normalized final times of optimal trajectories vary between about $\tau_f = 4.0$ at $\bar{\rho} = 0.5$ to about $\tau_f = 10.0$ at $\bar{\rho} = 2$. This covers a time period of about 15 to 120 s based on Table 1. Over these time intervals, the point-mass model is adequate.

Different initial trajectory guesses are used in the optimization process. They all lead to similar optimal solutions if the process converges. Better initial guesses result in smoother converged trajectories. In the results presented later, $C_{L_{\text{cr}}} = 0.33$ is used, and other trajectory variables are selected based on their corresponding steady-state level flight values in zero wind for $\tau \in [0, \tau_{f_0}]$, where $\tau_{f_0} = -2\bar{x}_0/\bar{V}_0$. Occasionally, a cycle of a sinusoidal component over the initial time interval is superposed to the constant altitude as the initial guess, to help obtain smooth converged trajectories, where the magnitude of the sinusoidal component is $(0.125\text{–}0.25)\bar{h}_0$.

VII. Patterns of Optimal Flights

Extensive numerical solutions suggest that patterns of optimal flights are mainly determined by $\bar{\rho}$, $\bar{\Gamma}$, and $\bar{h}_0$. Other parameters can modify the trajectory shapes and benefits. For small $\bar{\Gamma}$ or mild downbursts, optimal UAV flights stay in the two-dimensional vertical plane. When the downdraft becomes sufficiently strong or $\bar{\Gamma}$ is sufficiently large, three-dimensional maneuvers start to produce bigger fuel-saving benefits than 2-D vertical flights, though both are better than the straight-line reference flight. This critical $\bar{\Gamma}$ varies with $\bar{\rho}$. Furthermore, there is a maximum $\bar{\Gamma}$ for a given $\bar{\rho}$, beyond which the vehicle will not be able to recover from a downburst penetration without violating the constraints and the computer program does not converge.

The paper first focuses on two-dimensional flights in the vertical plane. This is achieved by imposing tight bounds on the bank angle and its rate $\mu_{\max} = 0.5$ deg and $|\dot{\mu}| \le \mu_{\max}/8$. Four basic patterns of optimal UAV flights in the vertical plane are identified, as shown in Fig. 3. A specific pattern depends on the relative initial altitude with respect to the height of the primary vortex ring. In these figures, the small circles in the altitude plots illustrate positions of the ring core and their radii are 10 times the core radius used in the optimization.

Unless otherwise noted, results below are obtained with $C_{D_0} = 0.025$, $E_{\max} = 15$, $\bar{\rho} = 1$, $\bar{\Gamma} = 1$, and $\bar{H} = 1$.

A. Optimal Jet-Engined UAV Flights

1) Pattern A occurs when the initial altitude is below the primary ring. In this case, the vehicle would descend and fly close to the ground until it passes through the central part of the downburst. In doing so, it flies through regions that have small downdrafts as well as a small horizontal wind shear. It would then climb and resume its original trajectory. For a certain range of normalized air densities and wind intensities, the UAV is able to perform this maneuver without using any thrust.

2) Pattern B results if the initial altitude is close to the height of the vortex ring. In this pattern, the vehicle would penetrate the vortex ring to use the downward flow to increase the kinetic energy. It flies above the ring core in its first encounter and then below the ring core in its second encounter. As a result, the horizontal wind component that the vehicle experiences is always tailwind, which can help to further increase its kinetic energy. For a certain range of $\bar{\rho}$ and $\bar{\Gamma}$, the vehicle is also able to accomplish this maneuver with zero thrust.

3) Pattern C is optimal when the initial altitude is adequately above the height of the vortex ring. In this maneuver, the vehicle would first descend and fly close to the ring core to take advantage of the updraft and the large tailwind. It would then climb to a relatively low downdraft region to pass through the central part of the downburst. Finally, the vehicle expends some of its energy to return to its original trajectory state toward the end by descending to fly closely above the ring core again. The entire trajectory stays above the vortex ring. Under appropriate conditions, the vehicle is able to fly this pattern with zero thrust.

4) Pattern D is optimal when the initial altitude is significantly higher than the height of the primary ring, where it would consume considerable energy to descend and then climb. In this case, the vehicle would simply climb to a higher altitude to cross the central part of the downburst at low downdraft flows, and then descend to return to its original flight state. Although this maneuver can save fuel compared with the straight-line reference trajectory or the turning avoidance trajectory, it always requires some thrust to accomplish.

The critical initial altitudes at which one pattern becomes more optimal than another depend on values of $\bar{\rho}$ and $\bar{\Gamma}$. In general, patterns B and C are sensitive to $\bar{h}_0$, $\bar{\rho}$, and $\bar{\Gamma}$. Pattern B is particularly so. In contrast, patterns A and D remain robust to initial altitudes in a wide range and are thus more feasible for practical implementations.

The corresponding airspeed and thrust of the four patterns are shown in Fig. 4. Basically, the airspeed varies in an opposite fashion as the altitude, while their combined motion enhances the energy intake. Peak normalized airspeeds are about 1.5 and reach 2.0 occasionally. For patterns A, C, and D, the thrust is only used over some segments of the entire trajectory. Different patterns differ in the time segment over which thrust is employed. For the dimensionless parameters used in obtaining these example trajectories, pattern B requires zero thrust. Over the ranges of the assumed parameter variations, all patterns A, B, and C have the potential of using zero

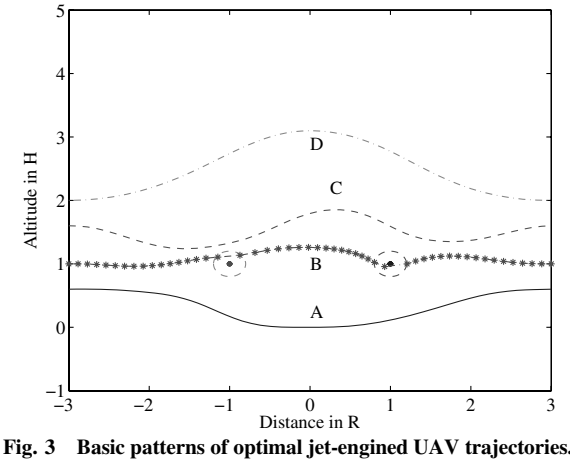

Fig. 3 Basic patterns of optimal jet-engined UAV trajectories.

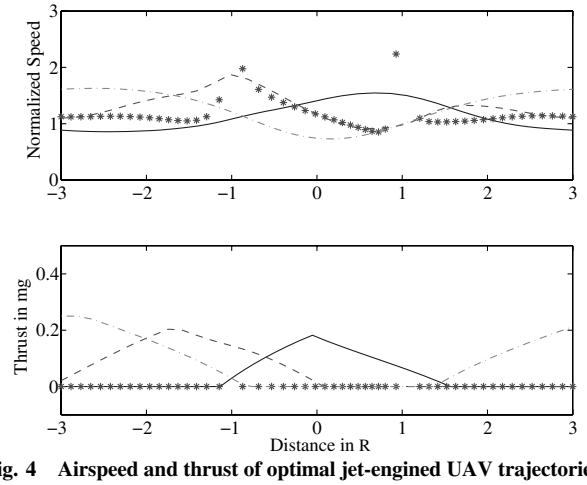

Fig. 4 Airspeed and thrust of optimal jet-engined UAV trajectories.

Table 2 Normalized flight times

$\bar{h}_0$	Pattern	τ_f
——	Straight-line reference	5.196
0.6	Pattern A	5.827
1.0	Pattern B	5.206
1.6	Pattern C	5.237
2.0	Pattern D	5.556

thrust for appropriate parameter combinations, whereas pattern D always requires some thrust at the beginning and toward the end of the trajectory. These figures also illustrate the drastic maneuvers required of a UAV in using downdraft winds, which may not be attempted by inhabited vehicles.

Table 2 shows normalized flight times corresponding to the different patterns in Figs. 3 and 4, for $\bar{\rho} = 1$. These flight times do not differ significantly from each other and from the straight-line reference trajectory flight time. For $R = 500$–5000 ft, these correspond to actual flight times from 20 to 72 s. Optimal flight times do change with $\bar{\rho}$, as discussed next.

B. Optimal Propeller-Driven UAV Flights

Optimal flights of a propeller-driven UAV through a downdraft exhibit almost the same basic patterns as those for a jet-engined UAV (Fig. 5). Because a propeller-driven UAV needs to minimize its power expenditures instead of the thrust as for a jet-engined UAV, the corresponding engine activities are somewhat different (Figs. 4 and 6).

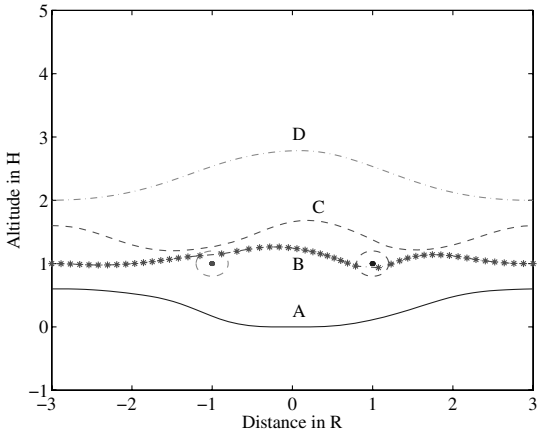

Fig. 5 Patterns of optimal propeller-driven UAV trajectories.

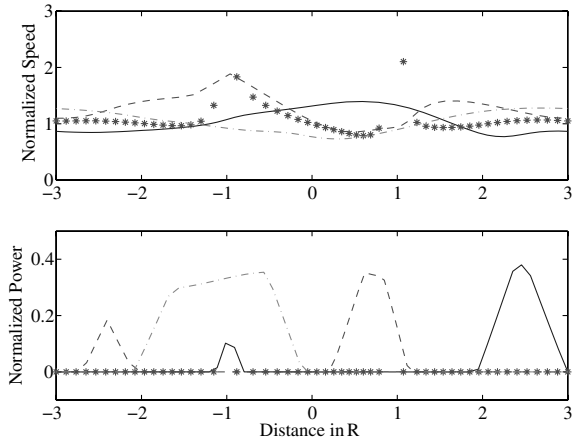

Fig. 6 Airspeed and power of optimal propeller-driven UAV trajectories.

C. Variations of Basic Patterns

Under some combinations of $\bar{\rho}$, $\bar{\Gamma}$, and $\bar{h}_0$, especially for larger values of $\bar{\rho}$, two of the four basic patterns can exhibit interesting variations. In Figs. 7 and 8, pattern A_s is obtained with $\bar{\rho} = 2$, $\bar{\Gamma} = 1$, and $\bar{h}_0 = 0.6\bar{H}$, whereas pattern C_s is obtained with $\bar{\rho} = 2$, $\bar{\Gamma} = 2$, and $\bar{h}_0 = 2\bar{H}$. Pattern A_s is a special variation of pattern A. In comparison, a vehicle would switch from pattern D to C_s or vice versa at different parameter combinations.

In pattern A_s, the vehicle flies close to the ring core from underneath in its first encounter, where it makes a rapid vertical turn by exploiting the high wind speed near the ring core. In pattern C_s, the vehicle flies closely to the ring core from above in its second encounter to similarly use the high wind speed to rapidly change its acceleration. Both variational patterns achieve zero thrust by taking advantage of the detailed wind pattern nearby a downburst core. They sensitively depend on an accurate knowledge of the downburst ring geometry and intensity.

D. Effects of $\bar{H}$

To examine the effect of different $\bar{H}$ on optimal flights, extensive numerical solutions are also obtained for two additional values of $\bar{H}$: 0.5 and 2. $\bar{H} = 0.5$ represents a low downburst that is closer to the ground, whereas $\bar{H} = 2$ represents a high downburst that is farther up from the ground. Results indicate that basic patterns of optimal flights remain similar for different values of $\bar{H}$. In addition, these patterns occur at similar normalized initial altitudes relative to $\bar{H}$ regardless of the value of $\bar{H}$. On the other hand, variations of $\bar{H}$ do affect values of the performance index, or the benefit of fuel saving. These effects vary in a nonlinear fashion with respect to $\bar{H}$. Details are omitted.

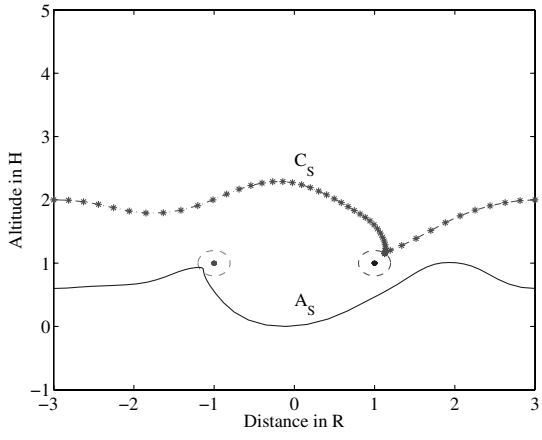

Fig. 7 Variations of basic optimal flight patterns.

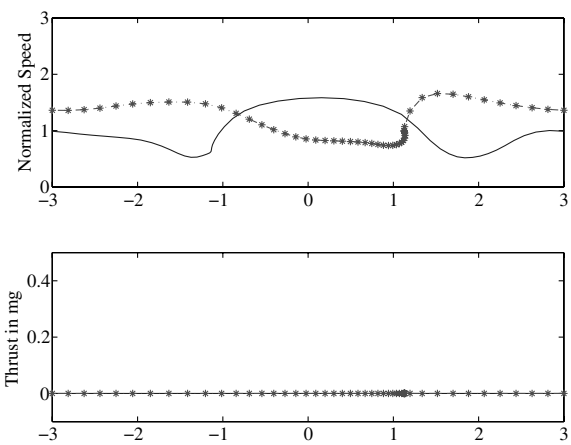

Fig. 8 Airspeed and thrust of variational optimal flight patterns.

E. Comparison of 2-D and 3-D Trajectories

Definitive trends of 3-D flight strategies are difficult to ascertain. Representative results are now shown on the differences between 2-D flights in the vertical plane and 3-D flights. Figures 9 and 10 depict optimal trajectories obtained with two sets of initial guesses. The first is the same as in the above to enforce 2-D flights in the vertical plane. The second assumes the initial bank angle $\mu(t)$ to be a sinusoidal function of time, being zero at the initial and final time, and reaching its maximum value $\mu_{\max}$ at the middle of the interval. In addition, bounds on lateral trajectory variables are relaxed in the corresponding trajectory optimization process to permit a 3-D flight: $\mu_{\max} = 40$ deg and $|\dot{\mu}| \leq \mu_{\max}/4$. Two initial altitudes are studied: $\bar{h}_0 = 0.6\bar{H}$ and $\bar{h}_0 = 2\bar{H}$.

For $\bar{h}_0 = 0.6\bar{H}$, the second initial guess leads to a 3-D optimal trajectory that avoids the central region of the downburst, whereas the first initial guess leads to a 2-D flight in the vertical plane. The 2-D flight uses some thrust in the middle of the flight when penetrating the central part of the downburst, whereas the 3-D flight requires zero thrust. In this case, the 3-D flight saves additional fuel compared with the 2-D flight. For $\bar{h}_0 = 2\bar{H}$, on the other hand, both initial guesses lead to the same optimal trajectory in the vertical plane, regardless of the bounds on lateral trajectory variables. In this case, the 2-D and the 3-D optimal trajectories are the same.

VIII. Performance Benefits of Optimal Flights Through Downdrafts

Potential fuel-saving benefits of optimal UAV flights through a downburst depend on values of the dimensionless parameters. We first examine the effect of the main performance parameter $\bar{\rho}$ using Eq. (24) for a jet-engined UAV. Under similar conditions, a smaller $\bar{\rho}$ corresponds to a larger wing loading or a larger vehicle and results in shorter flight times across a downburst.

The initial altitude of $\bar{h}_0 = 0.6\bar{H}$ corresponds to pattern A. As shown in Fig. 11a, the optimal value of the cost functional decreases or the fuel-saving benefit improves as $\bar{\Gamma}$ increases up to a certain point. Then, a further increase in $\bar{\Gamma}$ results in decreased benefit, and/or sometimes nonflyable wind fields. At $\bar{\rho} = 0.5$, the initial benefit increase as well as its subsequent decrease is gradual as $\bar{\Gamma}$ increases. At $\bar{\rho} = 1$, it becomes possible for the vehicle to use zero thrust to cross a downburst of adequate intensity. For a larger $\bar{\rho}$, the zero thrust trajectories start to appear at a smaller $\bar{\Gamma}$.

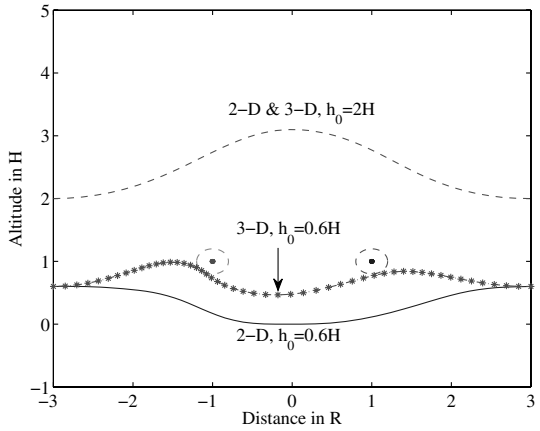

Fig. 9 Altitude of optimal 2-D and 3-D UAV trajectories.

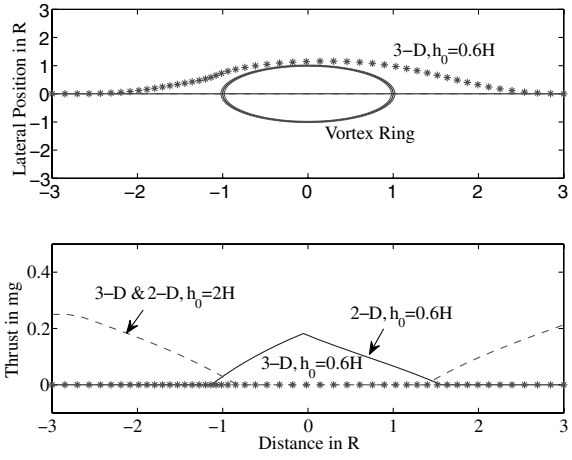

Fig. 10 Lateral position and thrust of 2-D and 3-D trajectories.

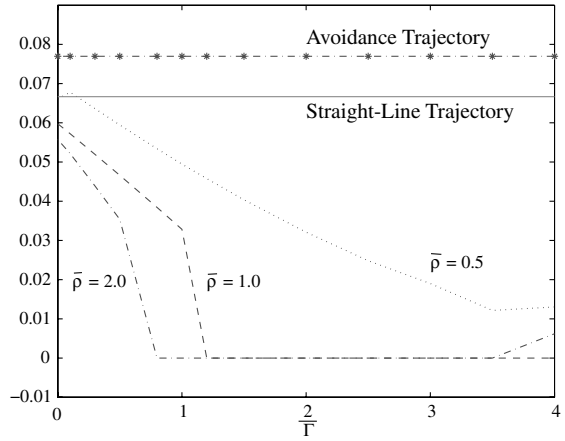

a)

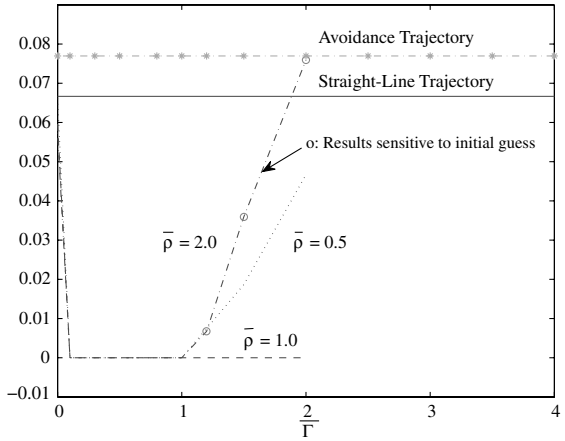

b)

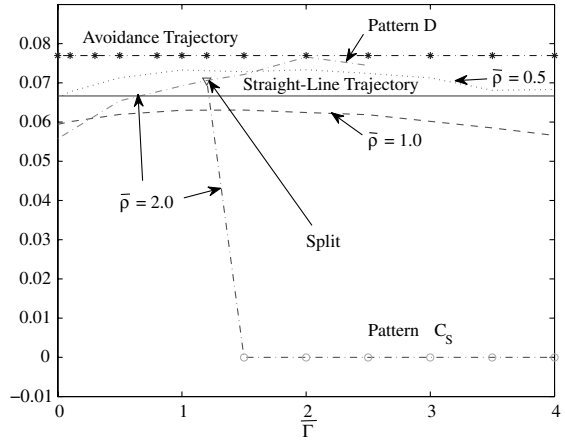

c)

Fig. 11 Optimal cost functional at a) $\bar{h}_0 = 0.6\bar{H}$, b) $\bar{h}_0 = \bar{H}$, and c) $\bar{h}_0 = 2.0\bar{H}$.

The initial altitude of $\bar{h}_0 = \bar{H}$ corresponds to pattern B, which is highly sensitive to variations of the dimensionless parameters. Figure 11b indicates that the fuel-saving benefit is small or the optimal cost functional value is large for very mild downburst winds or very smaller values of $\bar{\Gamma}$. As $\bar{\Gamma}$ increases, the optimal cost functional value quickly decreases or the fuel-saving benefit increases and reaches zero thrust. The cost functional value remains zero for a range of $\bar{\Gamma}$ until a certain point, beyond which further increases in $\bar{\Gamma}$ reduce the fuel benefit or increase the optimal cost functional value. As marked in Fig. 11b, calculated optimal cost functional values beyond this critical $\bar{\Gamma}$ are highly sensitive to parameter variations, revealing the sensitive nature of optimal trajectories of pattern B in strong downbursts.

Finally, trajectories with high initial altitudes correspond to pattern D. As shown in Fig. 11c, the fuel-saving benefit or the optimal cost functional value varies gradually as $\bar{\Gamma}$ increases for different values of $\bar{\rho}$. As $\bar{\Gamma}$ increases, the optimal cost functional value first increases and then decreases after reaching a peak. Correspondingly, the fuel-saving benefit first decreases and then increases as $\bar{\Gamma}$ increases. In general, the vehicle would climb higher for larger $\bar{\Gamma}$s or more intense downburst winds.

For $\bar{\rho} = 2$, however, the optimal cost functional value demonstrates an interesting split between patterns D and C_s. As $\bar{\Gamma}$ reaches a certain point, the variational pattern C_s starts to appear that results in zero thrust. If the standard pattern D is enforced in the numerical solution process through choices of initial guesses, the vehicle would use some thrust, and as $\bar{\Gamma}$ becomes larger, the corresponding optimal cost functional value follows the same trends as discussed in the previous paragraph.

Effects of aerodynamic parameters of a UAV on its fuel-saving benefit in flying through a downdraft are also studied. Overall, variations of C_{D_0} and $E_{\max}$ do not fundamentally alter the basic patterns of optimal flights discussed above. They do influence the levels of fuel-saving benefits. Specifically as $E_{\max}$ increases under equal conditions of other parameters, the benefit increases. In comparison, the effect of C_{D_0} on the fuel benefit seems to be nonlinear. Details are omitted.

IX. Conclusions

This paper studies characteristics and fuel-saving benefits of optimal flights of UAVs through downdraft flows. UAV motions are described by a point-mass dynamic model, and the downdraft flowfield is modeled by a pair of ring vortices placed symmetrically with respect to the ground. Equations of motion and downdraft wind expressions are normalized, and five fundamental dimensionless parameters are identified that govern UAV flights through a downdraft. UAV flights across downdrafts are formulated as nonlinear optimal control problems that minimize the average thrust per unit time for a jet-engined UAV or the average power per unit time for a propeller-driven UAV, both with open final time, open initial airspeed, and appropriate boundary conditions. A collocation method is used to convert these problems into parameter optimization for numerical solutions.

Four basic patterns of optimal two-dimensional UAV flights through downdrafts in the vertical plane are discovered. The initial vehicle altitude with respect to the height of the vortex ring determines which pattern is optimal. Pattern A results when the initial altitudes are lower than the vortex ring. In this pattern, the vehicle would descend and fly close to the ground until it passes the central part of the downdraft. When the initial altitudes are close to the height of the ring, pattern B occurs in which the vehicle would fly above the ring core in its first encounter and below the ring core in the second encounter, penetrating the primary vortex ring. As the initial altitude further increases above the primary ring, pattern C occurs. In this pattern, the vehicle flies above the ring vortex. It would descend and fly close to the ring core in its first encounter, then climb over the central part of the downdraft, and then fly close to the core again in its second encounter. This results in a sinusoidal altitude pattern that takes advantage of both the updraft outside of the ring and the tailwind. When the initial altitudes become even higher, pattern D results in which the vehicle would climb over the central part of the downdraft to fly through a region with relatively low downward wind speeds, and then descend to return to its original flight path after the downdraft is crossed. Under appropriate combinations of dimensionless parameters and the initial altitude, patterns A, B, and C require zero thrust. In comparison, pattern D would always require some fuel burn to complete though it can save fuel compared with a steady-state level flight or level turning avoidance flight.

Overall, optimal two-dimensional flights for a wide range of downdraft intensities always save fuel compared with the straight-line steady-state flight or the steady turning avoidance flight. Different combinations of dimensionless parameters and the initial altitude result in different optimal flight patterns and different levels of fuel savings. As the normalized downdraft intensity increases to a certain point, its further increase will either offer no improvement in the fuel savings or make it infeasible for the vehicle to fly through. In these cases, it is better for the UAV to avoid the downdraft. Under appropriate parameter conditions, three-dimensional flights through a downdraft provide additional fuel savings over two-dimensional flights in the vertical plane.

Acknowledgment

This work is supported in part by the National Science Foundation under award no. CCF-0515009.

References

[1] Pierson, B. L., and de Jong, J. L., "Cross-Country Sailplane Flight as a Dynamic Optimization Problem," *International Journal for Numerical Methods in Engineering*, Vol. 12, No. 11, 1978, pp. 1743–1759. doi:10.1002/nme.1620121111

[2] Pierson, B. L., and Chen, I., "Minimum Landing-Approach Distance for a Sailplane," *Journal of Aircraft*, Vol. 16, No. 4, 1979, pp. 287–288. doi:10.2514/3.58520

[3] de Jong, J. L., "Instationary Dolphin Flight: The Optimal Energy Exchange Between a Sailplane and Vertical Currents in the Atmosphere," *Optimal Control Applications and Methods*, Vol. 6, No. 2, 1985, pp. 113–124. doi:10.1002/oca.4660060205

[4] Lorenz, J., "Numerical Solution of the Minimum-Time Flight of a Glider Through a Thermal by Use of Multiple Shooting Methods," *Optimal Control Applications and Methods*, Vol. 6, No. 2, 1985, pp. 125–140. doi:10.1002/oca.4660060206

[5] Jenkins, S. A., and Wasyl, J., "Optimization of Glides for Constant Wind Fields and Course Headings," *Journal of Aircraft*, Vol. 27, No. 7, 1990, pp. 632–638. doi:10.2514/3.25333

[6] Bridges, P. D., "Alternative Solution to Optimum Gliding Velocity in a Steady Head Wind to Tail Wind," *Journal of Aircraft*, Vol. 30, No. 5, 1993, pp. 795–797. doi:10.2514/3.46415

[7] Qi, Y. C., and Zhao, Y. J., "Energy-Efficient Trajectories of Unmanned Aerial Vehicles Flying Through Thermals," *Journal of Aerospace Engineering*, Vol. 18, No. 2, April 2005, pp. 84–92. doi:10.1061/(ASCE)0893-1321(2005)18:2(84)

[8] Metzger, D. E., and Hedrick, J. K., "Optimal Flight Paths for Soaring Flight," *Journal of Aircraft*, Vol. 12, No. 11, Nov. 1975, pp. 867–871. doi:10.2514/3.59886

[9] Sachs, G., Knoll, A., and Lesch, K., "Optimal Utilization of Wind Energy for Dynamic Soaring," *Technical Soaring*, Vol. 15, No. 2, 1991, pp. 48–55.

[10] Zhao, Y. J., "Optimal Patterns of Glider Dynamic Soaring," *Optimal Control Applications and Methods*, Vol. 25, No. 2, 2004, pp. 67–89. doi:10.1002/oca.739

[11] Zhao, Y. J., and Qi, Y. C., "Minimum Fuel Powered Dynamic Soaring of Unmanned Aerial Vehicles Utilizing Wind Gradient," *Optimal Control Applications and Methods*, Vol. 25, No. 5, 2004, pp. 211–233. doi:10.1002/oca.744

[12] Miele, A., Wang, T., and Melvin, W. W., "Optimal Take-Off Trajectories in the Presence of Windshear," *Journal of Optimization Theory and Applications*, Vol. 49, No. 1, April 1986, pp. 1–45. doi:10.1007/BF00939246

[13] Miele, A., Wang, T., and Melvin, W. W., "Penetration Landing

Guidance Trajectories in the Presence of Windshear," *Journal of Guidance, Control, and Dynamics*, Vol. 12, No. 6, 1989, pp. 806–814. doi:10.2514/3.20485

[14] Psiaki, M. L., and Stengel, R. F., "Optimal Flight Paths Through Microburst Wind Profiles," *Journal of Aircraft*, Vol. 23, No. 8, Aug. 1986, pp. 629–635. doi:10.2514/3.45354

[15] Psiaki, M. L., and Stengel, R. F., "Analysis of Aircraft Control Strategies for Microburst Encounter," *Journal of Guidance, Control, and Dynamics*, Vol. 8, No. 5, Sept.–Oct. 1985, pp. 553–559. doi:10.2514/3.20022

[16] Zhao, Y., and Bryson, A. E., Jr., "Optimal Paths Through Downbursts," *Journal of Guidance, Control, and Dynamics*, Vol. 13, No. 5, Sept.–Oct. 1990, pp. 813–818. doi:10.2514/3.25406

[17] Zhao, Y., and Bryson, A. E., Jr., "Approach Guidance in a Downburst," *Journal of Guidance, Control, and Dynamics*, Vol. 15, No. 4, July–Aug. 1992, pp. 893–900. doi:10.2514/3.20922

[18] Kiceniuk, T., "Calculating the Benefits of Dynamic Soaring," *Technical Soaring*, Vol. 26, No. 1, Jan. 2002, pp. 17–26, http://soaringweb.org/Soaring_Index/Technical_Soaring/Technical_Soaring_issue.html.

[19] Boslough, M. B. E., "Autonomous Dynamic Soaring Platform for Distributed Mobile Sensor Arrays," Sandia National Laboratories Rept. SAND2002-1896, June 2002.

[20] Roach, J., "NASA Mini-Plane Holds Promise for Mars, Military," *National Geographic News*, 7 April 2006, http://news.nationalgeographic.com/news/.

[21] Fujita, T. T., *The Downburst*, Satellite and Meso-Meterology Research Project (SMRP), Department of Geophysical Sciences, University of Chicago, Chicago, IL, 1985, Chaps. 5–6.

[22] Arbuckle, P. D., Lewis, M. S., and Hinton, D. A., "Airborne Systems Technology Application to the Windshear Threat," *20th Congress of International Council of the Aeronautical Sciences*, International Council of the Aeronautical Sciences (ICAS), 1996, pp. 1640–1650; also Paper 96-5.7.1, 1996.

[23] Lamb, H., *Hydrodynamics*, 6th ed., Dover Publications, New York, 1932, pp. 236–239.

[24] Zhao, Y. J., "Optimal Control of an Aircraft Flying Through a Downburst," Ph.D Thesis, Departmentof Aeronautics and Astronautics, Stanford University, Stanford, CA, 1989.

[25] Stengel, R. F., *Flight Dynamics*, Princeton Univ. Press, Princeton, NJ, 2004, Chaps. 2–3.

[26] Vinh, N. X., *Optimal Trajectories in Atmospheric Flight*, Elsevier, Amsterdam, 1981, Chap. 3.

[27] Jackson, M. R., Zhao, Y. J., and Slattery, R. A., "Sensitivity of Trajectory Prediction in Air Traffic Management," *Journal of Guidance, Control, and Dynamics*, Vol. 22, No. 2, 1999, pp. 219–228. doi:10.2514/2.4398

[28] Hull, D. G., *Fundamentals of Airplane Flight Mechanics*, Springer, New York, 2007, Chap. 2.

[29] Anderson, J. D., Jr., *Introduction to Flight*, 5th ed., McGraw–Hill, New York, 2005, Secs. 6.12, 6.13.

[30] Betts, J., "Survey of Numerical Methods for Trajectory Optimization," *Journal of Guidance, Control, and Dynamics*, Vol. 21, No. 2, 1998, pp. 193–207. doi:10.2514/2.4231

[31] Hargraves, C. R., and Paris, S. W., "Direct Trajectory Optimization Using Nonlinear Programming and Collocation," *Journal of Guidance, Control, and Dynamics*, Vol. 10, No. 4, July–Aug. 1987, pp. 338–342. doi:10.2514/3.20223

[32] Herman, A. L., and Conway, B. A., "Direct Optimization Using Collocation Based on High-Order Gauss-Lobatto Quadrature Rules," *Journal of Guidance, Control, and Dynamics*, Vol. 19, No. 3, May–June 1996, pp. 592–599. doi:10.2514/3.21662

[33] Hull, D. G., "Conversion of Optimal Control Problems into Parameter Optimization Problems," *Journal of Guidance, Control, and Dynamics*, Vol. 20, No. 1, 1997, pp. 57–60. doi:10.2514/2.4033

[34] Fahroo, F., and Ross, I. M., "Direct Trajectory Optimization by a Chebyshev Pseudospectral Method," *Journal of Guidance, Control, and Dynamics*, Vol. 25, No. 1, Jan.–Feb. 2002, pp. 160–166. doi:10.2514/2.4862

[35] Huntington, G. T., and Rao, A. V., "Optimal Reconfiguration of Spacecraft Formations Using the Gauss Pseudospectral Method," *Journal of Guidance, Control, and Dynamics*, Vol. 31, No. 3, March–April 2008, pp. 689–698. doi:10.2514/1.31083

[36] Lu, P., "Use of Approximation Gradients in Trajectory Optimization," *Journal of Guidance, Control, and Dynamics*, Vol. 15, No. 5, 1992, pp. 1299–1301. doi:10.2514/3.20988

[37] Gill, P. E., Murray, W., and Saunders, M. A., "SNOPT: An SQP Algorithm for Large-Scale Constrained Optimization," Rept. NA 97-2, Department of Mathematics, Univ. of California, San Diego, CA, and Rept. SOL 97-3, Department of EESOR, Stanford University, Stanford, CA, 1997.

[38] Hale, F. J., *Introduction to Aircraft Performance, Selection, and Design*, Wiley, New York, 1984, p. 167.